Z. N. Cao

Y. M. Zhang
Mem. ASME

Center for Robotics and Manufacturing Systems
University of Kentucky,
Lexington, KY 40506

R. Kovacevic
Mem. ASME
Southern Methodist University,
Dallas, TX

Numerical Dynamic Analysis of Moving GTA Weld Pool

A three dimensional model with a moving heat source is developed to describe heat transfer and fluid flow in transient weld pools. Full penetration and free top and bottom surfaces are incorporated in the model in order to simulate the welding process more practically. The influence of plate thickness and welding current on the dynamics of weld pools is analyzed using calculated data. It is shown that when the workpiece is nearly penetrated, the depth of weld pool increases quickly. Also, the elevation of the top surface decreases quickly once the full penetration status is established.

1 Introduction

Many mathematical models have been established to describe heat transfer and fluid flow in weld pools [1–4]. However, most of the models were used to investigate the steady or quasi-steady state weld pools [4–11]. Only a few researchers considered the practical transient 3-D weld pools [12–14] and full penetration [15, 16]. However, the deformation of the bottom surface of the weld pool has been ignored. Full penetration is an important aspect of the welding process. When full penetration occurs, a new free surface is formed which affects the total behavior of the weld pool, including heat transfer, fluid flow, pool surface deformation, etc. Therefore, a transient analysis is performed for both partial and full penetration cases in this paper.

Penetration control is critical in obtaining sound welds. In order to achieve the desired full penetration state, the weld pool shape and size have been measured and used to control the gas tungsten arc (GTA) welding process [17, 18]. Also, it was found that a skilled human operator can extract the penetration information from the weld pool deformation [19, 20]. A novel approach has been proposed to measure the free 3D pool surface [21, 22]. Thus it is possible to control the welding process using the pool surface information. In order to develop a control system, the dynamics of the welding process, i.e., the transient characteristics, must be studied.

In this paper, a three-dimensional transient model of fluid flow and heat transfer is developed. Both the pool surface deformation and full penetration are considered in the model. In order to analyze the influence of welding parameters on the geometrical appearance of weld pools, a normalized model was used to characterize the geometrical appearance of weld pools. Interesting results have been obtained based on numerical calculations.

2 Numerical Calculation

2.1 Governing Equations. The following assumptions have been adopted for simplification:

(1) The arc is regarded as a spatially distributed heat, current, and pressure flux source.
(2) The flow is Newtonian, incompressible, and laminar.
(3) Physical properties are constant.

The coordinate system (x, y, z) is attached to the torch. The symmetric axis of the electrode is selected as the z axis. The work bottom surface is used to define the x-y plane and the torch travels along the x axis. The governing equations, described by the continuity equation, the momentum equation, and the energy equation for transient state velocity and temperature fields in the workpiece, may be written as follows:

$$\frac{\partial u}{\partial x} + \frac{\partial v}{\partial y} + \frac{\partial w}{\partial z} = 0 \tag{1}$$

$$\rho\left[\frac{\partial u}{\partial t} + u\frac{\partial u}{\partial x} + v\frac{\partial u}{\partial y} + w\frac{\partial u}{\partial z}\right] = F_x - \frac{\partial P}{\partial x} + \mu\left(\frac{\partial^2 u}{\partial x^2} + \frac{\partial^2 u}{\partial y^2} + \frac{\partial^2 u}{\partial z^2}\right) \tag{2}$$

$$\rho\left[\frac{\partial v}{\partial t} + u\frac{\partial v}{\partial x} + v\frac{\partial v}{\partial y} + w\frac{\partial v}{\partial z}\right] = F_y - \frac{\partial P}{\partial y} + \mu\left(\frac{\partial^2 v}{\partial x^2} + \frac{\partial^2 v}{\partial y^2} + \frac{\partial^2 v}{\partial z^2}\right) \tag{3}$$

$$\rho\left[\frac{\partial w}{\partial t} + u\frac{\partial w}{\partial x} + v\frac{\partial w}{\partial y} + w\frac{\partial w}{\partial z}\right] = F_z - \frac{\partial P}{\partial z} + \mu\left(\frac{\partial^2 w}{\partial x^2} + \frac{\partial^2 w}{\partial y^2} + \frac{\partial^2 w}{\partial z^2}\right) \tag{4}$$

$$\rho C_p\left[\frac{\partial T}{\partial t} + u\frac{\partial T}{\partial x} + v\frac{\partial T}{\partial y} + w\frac{\partial T}{\partial z}\right] = \frac{\partial}{\partial x}\left(K\frac{\partial T}{\partial x}\right) + \frac{\partial}{\partial y}\left(K\frac{\partial T}{\partial y}\right) + \frac{\partial}{\partial z}\left(K\frac{\partial T}{\partial z}\right) \tag{5}$$

where u, v, and w represent the x, y, and z directional velocities, respectively. t-time, ρ-density, K-thermal conductivity, μ-viscosity, C_p—specific heat, P—pressure, and T—temperature. F_x, F_y, and F_z are the components of the body force. The body force $\mathbf{F}$ is calculated using the electromagnetic and buoyancy force [9]:

$$\mathbf{F} = \mathbf{J} \times \mathbf{B} - \rho\beta\mathbf{g}(T - T_m) \tag{6}$$

Where $\mathbf{J}$ is the current density vector, $\mathbf{B}$—magnetic induction vector, β—coefficient of volume expansion, $\mathbf{g}$—gravitational acceleration vector, and T_m—melting temperature.

Contributed by the Manufacturing Engineering Division for publication in the JOURNAL OF MANUFACTURING SCIENCE AND ENGINEERING. Manuscript received Sept. 1995; revised Oct. 1996. Associate Technical Editor: S. G. Kapoor.

2.2 Boundary Conditions

(i) Top surface

$$-K\nabla T\cdot\mathbf{n}_t=\frac{\eta I u_w}{2\pi\sigma_q^2}\exp\left(-\frac{x^2+y^2}{2\sigma_q^2}\right)-q_{conv}-q_{radi}-q_{evap} \quad (7)$$

$$-\mu\nabla(\mathbf{V}_t\cdot\mathbf{t}_{tx})\cdot\mathbf{n}_t=\frac{\partial\gamma}{\partial T}\nabla T\cdot\mathbf{t}_{tx} \quad (8)$$

$$-\mu\nabla(\mathbf{V}_t\cdot\mathbf{t}_{ty})\cdot\mathbf{n}_t=\frac{\partial\gamma}{\partial T}\nabla T\cdot\mathbf{t}_{ty} \quad (9)$$

$$\mathbf{V}_t\cdot\mathbf{n}_t=0 \quad (10)$$

where $\mathbf{n}_t$ is the normal unit vector of the top surface, u_w—arc voltage, σ_q—arc heat flux distribution parameter, η—arc efficiency, $\mathbf{V}_t$—velocity vector on the top surface, $\mathbf{t}_{tx}$—the tangential unit vector of the top surface parallel to the $x-z$ plane, $\mathbf{t}_{ty}$—the tangential unit vector of the top surface parallel to the $y-z$ plane, and $\partial\gamma/\partial T$—temperature coefficient of the surface tension. The heat loss of convection, radiation and evaporation, i.e., q_{conv}, q_{radi} and q_{evap} can be written as:

$$q_{conv}=h(T-T_\infty) \quad (11)$$

$$q_{radi}=\sigma\epsilon(T^4-T_\infty^4) \quad (12)$$

$$q_{evap}=\dot{m}L_{evap} \quad (13)$$

where h is the convection coefficient, σ—Stefan-Boltzman constant, ϵ—surface emittance, T_∞—ambient temperature, L_{evap}—latent heat for the liquid-vapor phase-change, and $\dot{m}$—evaporation mass rate. For a metal, such as steel, $\dot{m}$ can be written as [23]:

$$\log(\dot{m})=A-B/T-0.5\log T \quad (14)$$

where A and B are two constants depending on material.

(ii) Bottom surface

$$-K\nabla T\cdot\mathbf{n}_b=-q_{conv}-q_{radi} \quad (15)$$

$$-\mu\nabla(\mathbf{V}_b\cdot\mathbf{t}_{bx})\cdot\mathbf{n}_b=\frac{\partial\gamma}{\partial T}\nabla T\cdot\mathbf{t}_{tb} \quad (16)$$

$$-\mu\nabla(\mathbf{V}_b\cdot\mathbf{t}_{by})\cdot\mathbf{n}_b=\frac{\partial\gamma}{\partial T}\nabla T\cdot\mathbf{t}_{by} \quad (17)$$

$$\mathbf{V}_b\cdot\mathbf{n}_b=0 \quad (18)$$

where $\mathbf{n}_b$ is the normal unit vector of the bottom surface, $\mathbf{V}_b$—velocity vector on the bottom surface, $\mathbf{t}_{bx}$—the tangential unit vector of the bottom surface parallel to $x-z$ plane, and $\mathbf{t}_{by}$—the tangential unit vector of the bottom surface parallel to the $y-z$ plane. Eqs. (10) and (18) are based on the assumption, that the transient variation of the free surface is slight so that the normal velocity on the free surface is approximately zero.

(iii) Pool Surface Deformation

The molten pool is distorted by the gravitational force and arc pressure. The surface tension acts to support the molten pool. For the arc-pool interface, i.e., the top pool surface, the static force balance can be described by [24]:

$$P_a-\rho g\phi+c=-\gamma\frac{(1+\phi_y^2)\phi_{xx}-2\phi_x\phi_y\phi_{xy}+(1+\phi_x^2)\phi_{yy}}{(1+\phi_x^2+\phi_y^2)^{3/2}} \quad (19)$$

where $z=L-\phi(x,y)$ is the top pool surface, L is the material thickness, γ is the surface tension, and $\phi_x=(\partial\phi/\partial x)$, $\phi_{xx}=\partial^2\phi/\partial x^2$. The arc pressure P_a is determined using the following formula [26]:

$$P_a(x,y)=\frac{\mu_0 I^2}{4\pi\sigma_j}\exp\left(-\frac{x^2+y^2}{2\sigma_j^2}\right) \quad (20)$$

I is the welding current, σ_j—arc current distribution parameter, and μ_0—magnetic permeability. When the weld pool is fully penetrated, the bottom pool surface is also deformed. On the bottom pool surface, the surface tension prevents the weld pool from being burnt-through. The balance between gravity and surface tension can be written as [24]:

$$\rho g(\psi+L-\phi)-c=-\gamma\frac{(1+\psi_y^2)\psi_{xx}-2\psi_x\psi_y\psi_{xy}+(1+\psi_x^2)\psi_{yy}}{(1+\psi_x^2+\psi_y^2)^{3/2}} \quad (21)$$

Nomenclature

a, b = model parameters of geometrical appearance of the weld pool
$\mathbf{B}$ = magnetic induction vector
C_p = specific heat
F_x, F_y, F_z = component of body force
$\mathbf{g}$ = gravitational acceleration vector
I = welding current
$\mathbf{J}$ = current density vector
K = thermal conductivity
L = thickness of specimen
l = length of weld pool
L_{evap} = latent heat for the liquid-vapor phase change
$\dot{m}$ = evaporation mass rate
$\mathbf{n}_b$ = normal unit vector to bottom surface
$\mathbf{n}_t$ = normal unit vector to top surface
p = liquid pressure
P_a = arc pressure
q_{conv} = heat loss from convection
q_{evap} = heat loss from evaporation
q_{radi} = heat loss from radiation
r = radial distance
T = temperature
T_m = melting temperature
T_∞ = ambient temperature
t = time
$\mathbf{t}_{bx}$ = tangential unit vector of bottom surface parallel to x-z plane
$\mathbf{t}_{by}$ = tangential unit vector of bottom surface parallel to y-z plane
$\mathbf{t}_{tx}$ = tangential unit vector of top surface parallel to x-z plane
$\mathbf{t}_{ty}$ = tangential unit vector of top surface parallel to y-z plane
u = x-direction velocity
u_m = arc voltage
u_0 = welding speed
$\mathbf{V}_b$ = velocity vector of bottom surface
$\mathbf{V}_t$ = velocity vector of top surface
v = y-direction velocity
w = z-direction velocity
w_r = relative pool width
x, y, z = regular coordinate system
x_r, y_r = normalized coordinate system
x_0 = position of maximum pool width μ = viscosity
μ_0 = magnetic permeability
ρ = density
β = coefficient of volume expansion
γ = surface tension
$\partial\gamma/\partial T$ = surface tension temperature coefficient
η = arc efficiency
σ = Stefan-Boltzmann constant
σ_j = arc current flux distribution parameter
σ_q = arc heat flux distribution parameter
ϵ = surface emittance
ϕ = shape function of top pool surface
ψ = shape function of bottom pool surface

Table 1 Parameters used in computation

$C_p = 630J/kg \cdot K$	$\mu = 6 \times 10^{-3} kg/m \cdot s$
$h = 80w/m^2 \cdot K$	$\mu_0 = 1.26 \times 10^{-6} H/m$
$K = 22w/m \cdot K$	$\rho = 7200kg/m^3$
$L = 3 \times 10^{-3} m$	$\beta = 1 \times 10^{-4} K^{-1}$
$T_\infty = 300K$	$\gamma = 1.0N/m$
$T_m = 1723K$	$\partial\gamma/\partial T = -0.112 \times 10^{-3} N/mK$
$\varepsilon = 0.25$	$\eta = 0.65$

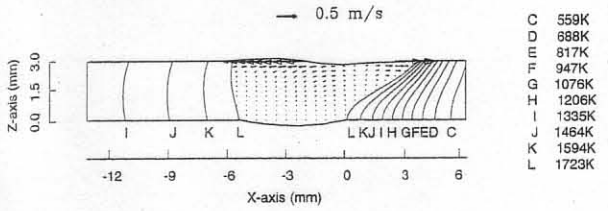

Fig. 1 Temperature distribution and fluid flow field in weld pool at the longitudinal section of workpiece

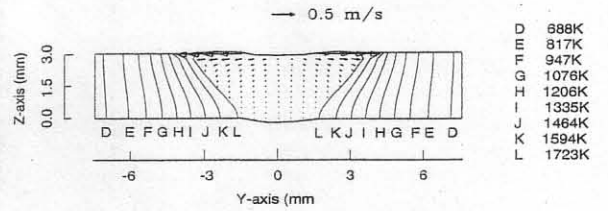

Fig. 2 Temperature distribution and fluid flow field in weld pool at the cross section of workpiece

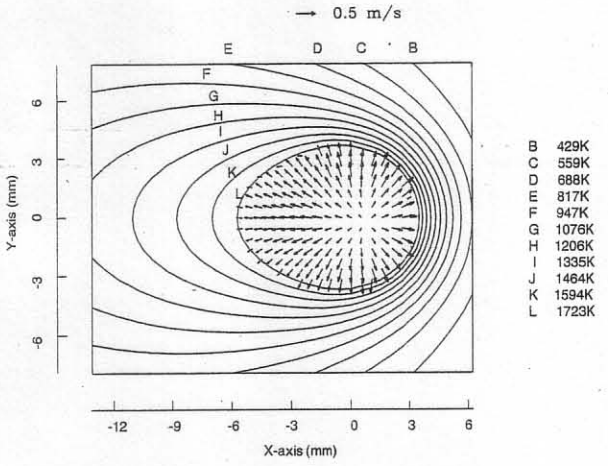

Fig. 3 Temperature distribution and fluid flow field at the top surface of workpiece

where $z = -\psi(x, y)$ is the bottom pool surface, and $\psi_x = (\partial\psi/\partial x)$, $\psi_{xx} = \partial^2\psi/\partial x^2$. The constant c can be determined from the following constraint of constant volume:

$$\iint \phi(x, y)dxdy - \iint \psi(x, y)dxdy = 0 \qquad (22)$$

Equations (19) and (21) have the following boundary conditions, respectively,

$$\phi(x, y) = 0, \quad \text{when} \quad T \le T_m \qquad (23)$$

$$\psi(x, y) = 0, \quad \text{when} \quad T \le T_m \qquad (24)$$

2.3 Numerical Solution. The governing equations with the boundary conditions are transformed into finite difference equations. In order to improve the accuracy of the calculation, grid with uneven spacing is used for the calculational domain. Finer spacing was used in the region where the arc passed because of the higher temperature gradient and fluid flow. The finest spacing was used in the thickness-direction in order to describe the deformed weld pool surface. The SIMPLER algorithm [27] is employed to calculate the temperature and fluid flow fields. Different welding parameters have been used in the calculation in order to analyze the effect of welding parameters on the geometry of weld pools. It is known that both σ_q and σ_j increase when the welding current or arc length is increased. In our calculation, the arc distribution parameters, i.e. σ_q and σ_j, have been selected for different welding current and arc length according to the experimental results [26]. Calculations are made for GTA weld pools on stainless steel plates. The parameters used in the computation are shown in Table 1.

The calculated three-dimensional temperature distribution and velocity field are shown in Figs. 1–3. It is found that for the full penetration pool, except for the pool edge, the molten metal on the surface flows radially outward and moves vertically upward in the neighborhood of the arc axis. That means that the pattern of convection in weld pool is mainly determined by the temperature coefficient of surface tension.

Figure 4 shows the three-dimensional shapes of the calculated top and bottom surfaces. It can be clearly seen that on the top surface, the molten metal is depressed in the arc affected region, whereas it is pushed upward and outward from the arc center in the non-depressed region. This result is consistent with our experimental observations [28]. On the bottom surface, it has

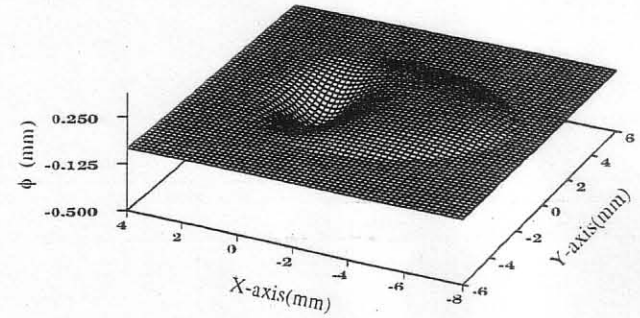

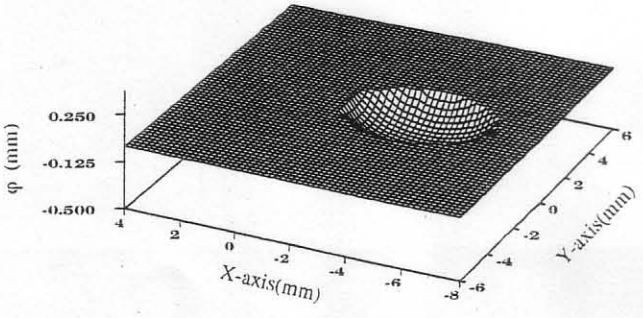

Fig. 4 Three dimensional weld pool surface. (*a*) top surface. (*b*) bottom surface. Current 120A, voltage 12V, torch speed 3.0 mm/s.

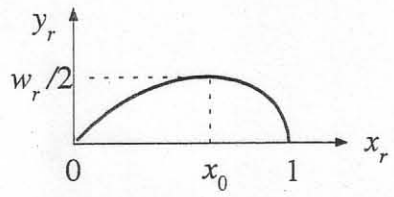

Fig. 5 Normalized coordinate system

been shown that the entire pool surface sags and a maximum sag exits at the center of the molten region.

3 Normalized Model of Weld Pool Geometry

In order to study the geometry of the weld pool, the weld pool must be characterized by parameters. The selection of the characteristic parameters is crucial. Three criteria must be satisfied. First, the fundamental geometrical appearance of the weld pool must be sufficiently described using the selected characteristic parameters. Secondly, the correlation between the status of the weld penetration and selected characteristic parameters must be substantial. Also, in the projected control system for weld penetration, the selected parameters must be controlled to achieve the desired weld pool and weld penetration. Although more parameters could describe the weld pool more accurately, the increase in the number of the selected characteristic parameters may complicate the resultant control system. Thus, the number of the selected parameters must not be too large.

We have proposed the following parametric model to describe the weld pool boundary in the normalized coordinate system $x_r o y_r$ (Fig. 5) [25]:

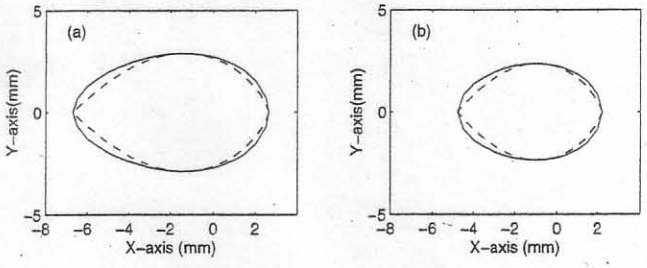

Fig. 6 Comparison between the numerical boundary and normalized one (— numerical, -- normalized). (*a*) 120A (*b*) 80A.

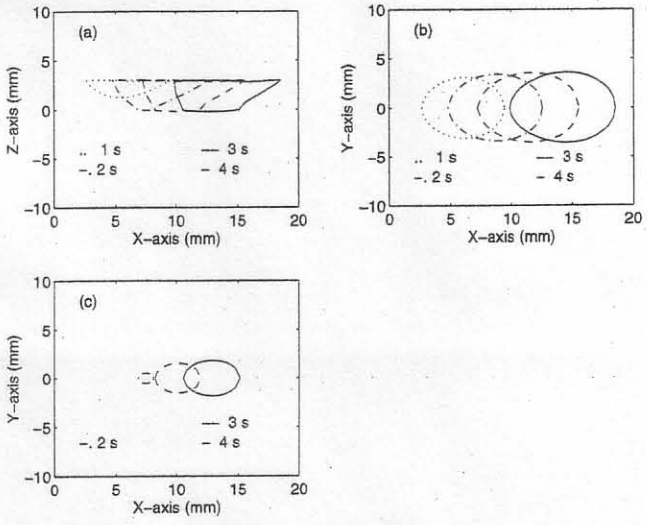

Fig. 7 Transient formation of weld pool (*a*) longitudinal section (*b*) top surface (*c*) bottom surface

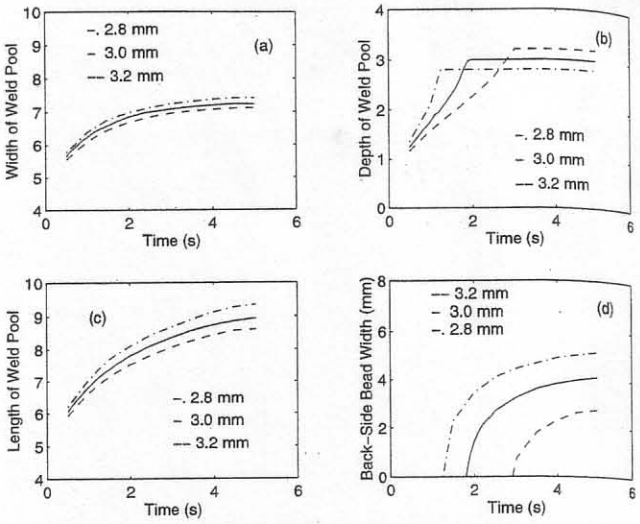

Fig. 8 The weld pool sizes verses welding time with different thickness of workpiece (*a*) width of weld pool (*b*) depth of weld pool (*c*) length of weld pool (*d*) backside bead width

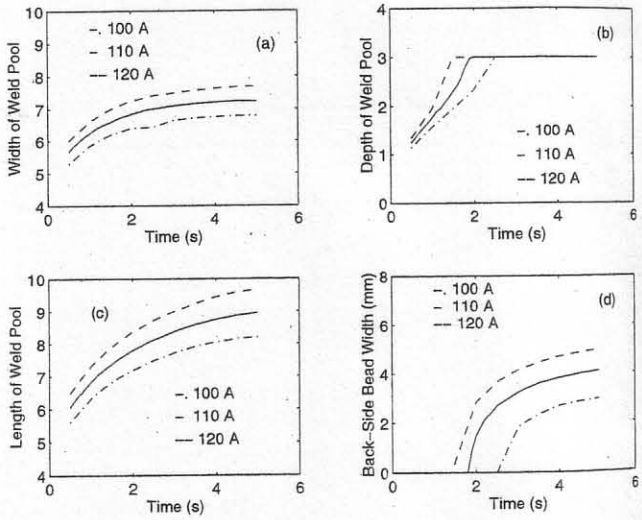

Fig. 9 The weld pool sizes versus welding time with different welding currents (*a*) width of weld pool (*b*) depth of weld pool (*c*) length of weld pool (*d*) back-side bead width

$$y_r = \mp a(1 - x_r)^b x_r \quad (a > 0,\ 1 \geq b > 0) \tag{25}$$

where $x_r = x/l$, $y_r = y/2l$, l is the length of the weld pool, and a and b are the model parameter. In Fig. 5, w_r is the relative pool width, and $y_r(x_0) = w_r/2$. Here x_0 characterizes the position where the pool is the widest, and $x_0 = b/(b + 1)$. The weld pool is therefore divided as the leading and trailing portions by $x = x_0$. Hence, x_0 can be used as a parameters to characterize a geometrical feature of the weld pool. It has been shown (Fig. 6) that the geometry of the weld pool can be sufficiently characterized using the parameters l, a, and b [25]. Also, the back-side bead width can be accurately calculated using l, a, and b [25]. Thus, these parameters are used to characterize the geometry of the weld pool.

4 Transient Analysis of Weld Pool

4.1 Weld Pool Size and Penetration. The weld pool sizes, i.e. the length, width, and depth, verses welding time are shown in Fig. 8 and Fig. 9 for different welding currents and workpiece thicknesses, respectively. It can be seen that the rate

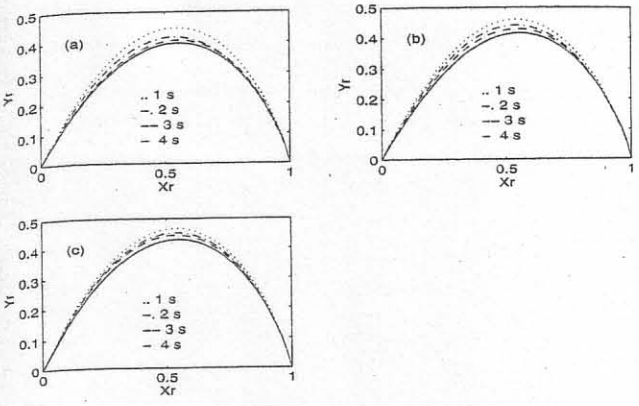

Fig. 10 Appearance geometries of weld pools with different thickness of workpiece at different instants (*a*) 2.5 mm (*b*) 3.0 mm (*c*) 3.5 mm

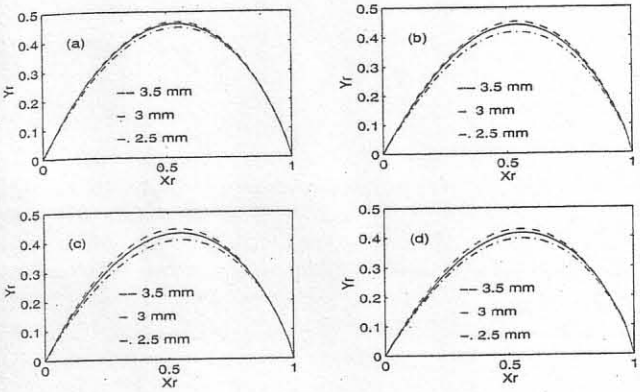

Fig. 11 Appearance geometries of weld pools with different thickness of workpiece at different instants (*a*) 1 s (*b*) 2 s (*c*) 3 s (*d*) 4 s

of increase in the weld pool size decreases as the time increases. However, the depth of penetration exhibits a different trend. Initially, the rate of depth increase is relatively small. When the workpiece is nearly penetrated, the weld pool depth increases quickly (Fig. 8(*b*) and Fig. 9(*b*)). Also, the back-side bead width of the weld pool increases very fast when the full penetration is just established (Fig. 8(*d*) and Fig. 9(*d*)). Similar results were observed by Burgardt and Heiple [29] from experiments. Referring to Fig. 8, when other conditions are the same, the size of the weld pool for a thinner workpiece is larger than with a thick workpiece. This is simply caused by the difference in the heat transfer condition.

4.2 Geometrical Shape. In order to analyze and compare the change in the geometrical shape of weld pools, the normalized models of weld pools with different thicknesses at different instants are shown in Fig. 10 and Fig. 11. From Fig. 10, it is seen that during the transition period, the width to length ratio of weld pools decreases. This is directly caused by the heat accumulation. Figure 11 shows that at any instant in the transition period, the width to length ratio of weld pools increases as the thickness increases. In fact, the width of the weld pool has more instantaneous correlation with the heat input than the pool length. The heat transfer condition does influence the pool width. However, because of a longer period of heat transfer, the heat transfer condition tends to influence the pool length more intensively. Thus, the width to length ratio should increase as the heat transfer condition becomes poor. The width to length ratio can also be illustrated using the relative width (Fig. 12). Figure 13 shows x_0 with the different thickness and welding current during the transient period. With the growth of the weld pool, x_0 moves towards the front. That is, the ratio between the leading and trailing portions decreases.

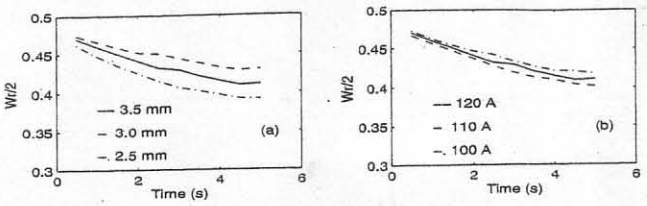

Fig. 12 Relative width during the growth of weld pool (*a*) with different thickness (*b*) with different current

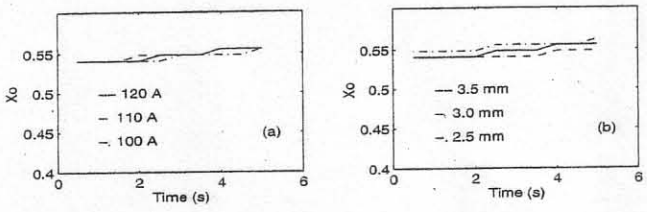

Fig. 13 The change in x_0 during the growth of weld pool (*a*) with different thickness (*b*) with different current

4.3 Weld Pool Deformation. The top and bottom free surfaces in the transient period are shown in Fig. 14. The maximum depression of the weld pool increases gradually. Before full penetration is established, a maximum elevation of weld pool surface is reached. Once the workpiece is penetrated, the elevation starts to decrease (shown in Fig. 15 and Fig. 16). Also, before the workpiece is penetrated, the depression volume nearly equals the elevation volume, i.e., the average deformation of top surface tends to equal zero. When the full penetration

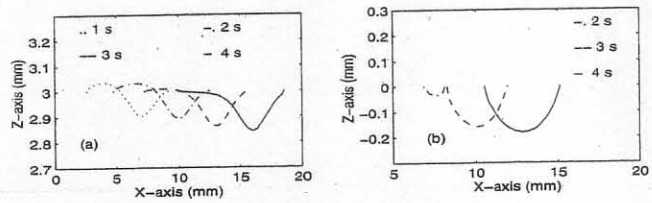

Fig. 14 The transient change of top and bottom free surface during weld pool formation (*a*) top surface (*b*) bottom surface

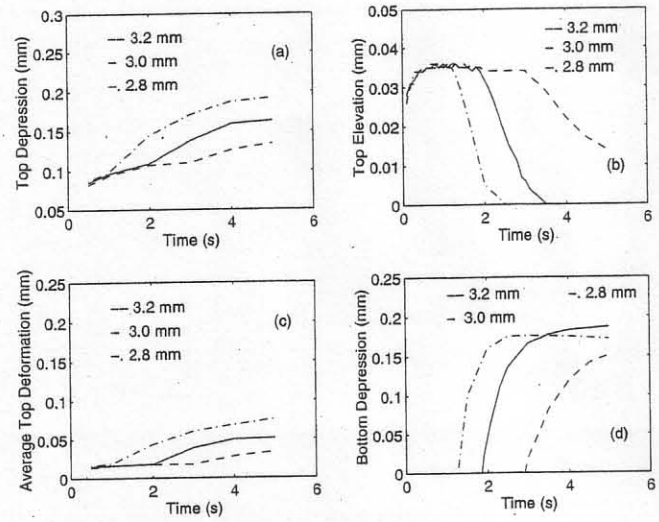

Fig. 15 The surface deformation of weld pools with the different thickness of workpiece at the different instants (*a*) maximum top depression (*b*) maximum top elevation (*c*) average top deformation (*d*) maximum bottom depression

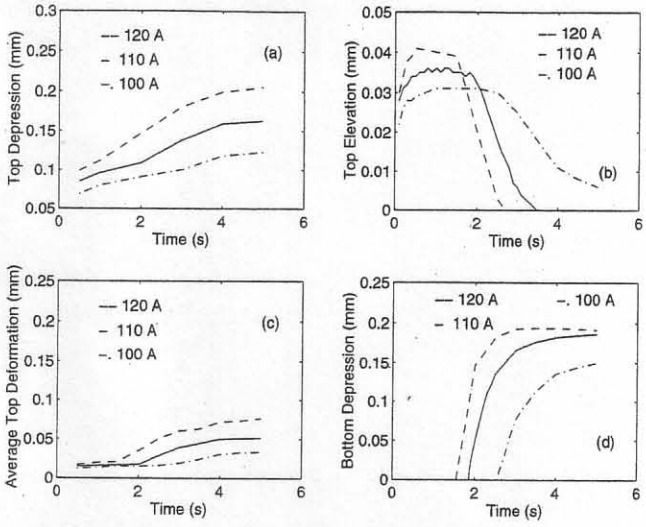

Fig. 16 The surface deformation of weld pools with the different welding currents at the different instants (*a*) maximum top depression (*b*) maximum top elevation (*c*) average top deformation (*d*) maximum bottom depression

status is reached, the depression and elevation quickly increases and decreases, respectively (see Fig. 15(*c*) and Fig. 16(*c*)). Thus, the depression and elevation volumes of the top surface become unequal. The average deformation starts to increase after full penetration occurs. Hence, the volume difference between the top surface depression and elevation, i.e., the average deformation on the top surface, contains the penetration information. In fact, once the full penetration is well established, the depression volumes on the top and bottom surfaces tend to be equal, whereas the elevation of the top surface tends to vanish. Therefore, the elevation of the top surface can provide the information about the penetration. When the elevation of the top surface starts to decrease, the workpiece must already be penetrated.

5 Conclusions

A three dimensional model has been developed to analyze the heat transfer and fluid flow in transient weld pools. Both the full penetration and free top and bottom surface have been considered in the model. Based on the numerical results, the following are found:

(1) The depth of the weld pool quickly increases as the pool approaches full penetration. Also, the back-side bead width of the weld pool increases very quickly when the full penetration is just established.

(2) During the growth of weld pools, the width-length ratio of weld pool decreases and the ratio between the leading and trailing portions decreases.

(3) Once the elevation of weld pool surface decreases quickly, the full penetration status must already be reached. The volume difference between the top surface depression and elevation also contains the penetration information.

Acknowledgments

This work is supported by the National Science Foundation (DMI-9634735) and Allison Engine Company, Indianapolis, IN and the Center for Robotics and Manufacturing Systems at the University of Kentucky.

References

1 Attey, D. R., 1980, "A Mathematical Model for Fluid Flow in a Weld Pool at High Current," *Journal of Fluid Mechanics,* Vol. 98, p. 787.

2 Oper, G. M., and Szekely, J., 1984, "Heat and Fluid Flow Phenomena in Weld Pools," *Journal of Fluid Mechanics,* Vol. 147, p. 53.

3 Kou, S., and Wang, Y. H., 1986, "Computer Simulation of Convection in Moving Arc Weld Pools," *Metall. Trans.,* Vol. 17A, p. 2271.

4 Tsao, K. C., and Wu, C. S., 1988, "Fluid Flow and Heat Transfer in GTA Weld Pools," *Weld. J.,* Vol. 67, 1988, p. 70s.

5 Kim, S. D., and Na, S. J., 1989, "A Study of Heat and Mass Flow in Stationary Gas Tungsten Arc Welding Using the Numerical Mapping Method," *Proc. Instn. Mech. Engrs. Part B Journal of Engineering Manufacture,* Vol. 203, p. 233.

6 Thompson, M. E., and Szekely, J., 1989, "The Transient Behavior of Weld Pools With a Deformed Free Surface," *Inter. J. of Heat and Mass Transfer,* Vol. 32, p. 1007.

7 Choo, R. T. C., and Szekely, J., 1990, "Modeling of High-Current Arc With Emphases on Free Surface Phenomena in the Weld Pool," *Weld. J.* Vol. 69, p. 223s.

8 Tsai, M. C., and Kou, S., 1989, "Marangoni Convection in Weld Pools With a Free Surface," *Inter. J. of Numerical Methods in Fluid,* Vol. 9, p. 1503.

9 Kim, S.-D., and Na, S.-J., 1994, "A Study on the Three-Dimensional Analysis of Heat and Fluid Flow in Gas Metal Arc Welding Using Boundary-Fitted Coordinates," ASME JOURNAL OF ENGINEERING FOR INDUSTRY, Vol. 116, p. 78.

10 Kim, S.-D., and Na, S.-J., 1992, "Effect of Weld Pool Deformation on Weld Penetration in Stationary Gas Tungsten Arc Welding," *Weld. J.,* Vol. 71, p. 179s.

11 Zacharia, T., et al., 1989, "Three-Dimensional Transient Model for Arc Welding Process," *Metall. Trans.,* Vol. 20B, p. 645.

12 Zacharia, T., et al. 1989, "Modeling of Non-Autogenous Welding," *Weld. J.,* Vol. 68, p. 18s.

13 Sheng, I. C., and Chen, Y., 1992, "Modeling Welding by Surface Heating," ASME *Journal of Engineering Materials and Technology,* Vol. 114, p. 439.

14 Chen, Y., and Sheng, I. C., 1993, "On the Solid-Liquid Transition Zone in Welding Analysis," ASME *Journal of Engineering Materials and Technology,* Vol. 115, p. 17.

15 Kou, S., and Wang, Y. H., 1986, "Computer Simulation of Convection Moving Arc Weld Pools," *Metal Trans.,* Vol. 17A, p. 2271

16 Zacharia, T., et al., 1995, "Surface Temperature Distribution of GTA Weld Pools on Thin-Plate 304 Stainless Steel," *Weld. J.,* Vol. 74, p. 353s.

17 Kovacevic, R., Zhang, Y. M., and Ruan, S., 1995, "Sensing and Control of Weld Pool Geometry for Automated GTA Welding," ASME JOURNAL OF ENGINEERING FOR INDUSTRY, Vol. 117, p. 210.

18 Kovacevic, R., Zhang, Y. M, and Li, Lin, "Monitoring of Weld Penetration Based on Weld Pool Appearance," *Welding Journal,* Vol. 75, 1996, p. 317s.

19 Zhang, Y. M., et al., 1993, "Determining Joint Penetration in GTAW With Vision Sensing of Weld-Face Geometry," *Weld. J.,* Vol. 72, p. 463s.

20 Zhang, Y. M., Kovacevic, R., and Wu, L., 1996, "Dynamic Analysis and Identification of Gas Tungsten Arc Welding Process for Full Penetration Control," ASME JOURNAL OF ENGINEERING FOR INDUSTRY, Vol. 118, No. 1, p. 123.

21 Kovacevic, R., Zhang, Y. M., and Ruan, S., 1993, "Three-Dimensional Measurement of Weld Pool Surface," *Proceedings of the International Conference on Modeling and Control of Joining Processes,* p. 607, Orlando, Florida, Dec. 8–10, ASM.

22 Zhang, Y., Beardsley, M., and Kovacevic, R., 1994, "Real-time Image Processing in 3D Measurement of Weld Pool Surface," *Manufacturing Science and Engineering,* PED-Vol. 68-1, p. 255, ASME. Also in ASME JOURNAL OF MANUFACTURING SCIENCE AND ENGINEERING, Vol. 119, No. 2, p. 161.

23 Choi, M., and Greif, R., 1987, "A Study of the Heat Transfer During Arc Welding With Applications to Pure Metals Temperature Materials," *Numerical Heat Transfer,* Vol. 11, p. 477.

24 Ohji, T., and Nishiguchi, K., 1983, "Mathematical Modeling of Molten Pool in Arc Welding of Thin Plate," IIW DOC.211-555-83.

25 Zhang, Y. M., Li, L., and Kovacevic, R., 1995, "Dynamic Correlation Between Weld Pool Shape and Weld Penetration," ASME *International Mechanical Engineering Congress,* MD Vol. 69-2, p. 883, 12–17 November, San Francisco, CA. Also in ASME JOURNAL OF MANUFACTURING SCIENCE AND ENGINEERING, Vol. 119, No. 4, p. 631.

26 Lin, M. L., and Eagar, T. W., 1986, "Pressure Produced by Gas Tungsten Arcs," *Metal Trans.,* Vol. 17B, p. 601.

27 Patankar, S. V., 1980, *Numerical Heat Transfer and Fluid Flow,* McGraw-Hill.

28 Kovacevic, R., and Zhang, Y. M., 1995, "Vision Sensing of 3D Weld Pool Surface," The 4th International Conference on Trends in Welding Research, 5–8 June, Gatlingburg, TN.

29 Burgardt, P., and Hiple, C. R., 1992, "Weld Penetration Sensitivity to Welding Variable When Near Full Joint Penetration," *Weld. J.,* Vol. 71, p. 341s.